

Ferromagnetic Polarons, Phase Separation, Stripes and Polaron Lattice: The two- and three-dimensional ferromagnetic Kondo Model

Maria Daghofer,¹ Winfried Koller,² Hans Gerd Evertz,¹ and Wolfgang von der Linden¹

¹*Institute for Theoretical and Computational Physics,
Graz University of Technology, Petersgasse 16, A-8010 Graz, Austria.**

²*Department of Mathematics, Imperial College, 180 Queen's Gate, London SW7 2BZ, UK.*

(Dated: October 10, 2003)

We investigate the two- and three-dimensional ferromagnetic Kondo lattice model by unbiased Monte Carlo simulations. A phase diagram for the two-dimensional model is presented, in which the stability of magnetic order and ferromagnetic polarons is examined with respect to the antiferromagnetic superexchange J' and temperature. The Monte Carlo simulations reveal that $J' \geq 0.02$ strengthens individual polarons while small $J' < 0.02$ favors larger clusters and phase separation except for small doping. Lowering the temperature stabilizes ferromagnetic polarons for realistic $J' \gtrsim 0.01$, while phase separation is only favored for very small $J' \lesssim 0.01$. Our Monte Carlo simulations show that low temperatures can lead to diagonal or vertical stripes depending on J' .

Simulations for three-dimensional systems yield ferromagnetic polarons, which form a 'polaron lattice' at higher doping levels $0.2 \lesssim x \lesssim 0.23$, when independent polarons do no longer fit into the system. No tendency to phase separation is observed in three dimensions.

I. INTRODUCTION

Doped and undoped manganese oxides, such as $R_{1-x}A_x\text{MnO}_3$, where R denotes a rare earth and A an alkaline earth, have a very complex phase diagram^{1,2} depending on temperature, doping, ionic radius of the involved elements or magnetization. They have been thoroughly investigated because of the CMR effect and have been found to have a rich phase diagram including ferromagnetic (FM), antiferromagnetic (AFM), insulating, metallic and charge ordered states. Quasi two-dimensional (2D) systems with well separated MnO_2 - (bi)layers exist.

A comprehensive understanding of their properties certainly requires treatment of the phononic degrees of freedom and of the orbital degeneracy including Coulomb repulsion, which however would pose overwhelming difficulties, especially in more than one dimension.

The much simpler FM Kondo lattice model³ captures some of the properties of these materials, namely the hopping of the itinerant manganese e_g electrons via the intermediate oxygen ions (double exchange) and their strong Hund's rule coupling to the $S = 3/2$ corespin formed by the localized manganese t_{2g} electrons. An additional antiferromagnetic coupling between the corespins is often included to account for superexchange of the t_{2g} electrons. Even for this model, full quantum mechanical calculations are difficult in more than one dimension, and it has therefore been proposed to replace the t_{2g} corespin by a classical spin.^{4,5,6} While this approximation has been criticized,^{7,8,9} it has been shown to yield good results at low but finite temperatures.⁵ As the ferromagnetic coupling J_H of the itinerant electrons to the corespins is far larger than the hopping strength or the antiferromagnetic superexchange J' , energy scales can be separated and the model can thereby be considerably simplified. In the customary $J_H \rightarrow \infty$ approach and in the second order per-

turbative treatment of the virtual excitations¹⁰ for large but finite J_H , it is assumed that the e_g electrons are parallel to the local corespin. Double occupancies are thus suppressed and Coulomb repulsion is usually neglected.

The FM Kondo lattice model with classical corespins has been extensively investigated.^{5,6,10,11,12,13,14,15,16,17,18,19} The influence of classical phonons^{20,21,22} and disorder^{23,24} has been addressed. Two-orbital models have been treated, mainly with classical phonons but without Coulomb repulsion. Aliaga *et al.* have examined the two-dimensional one-orbital Kondo model for $J_H \rightarrow \infty$ with an algorithm similar to ours¹⁹ and reported several phases (stripes, island phases for commensurate fillings, and the so called "Flux Phase") as well as phase separation (PS), which has also been related by other authors.^{5,12,14,20,25} Stripes were reported in a Kondo model applied to cuprates with different parameter values.^{26,27,28}

In previous papers,^{10,17,18} we have studied the one-dimensional model by Monte Carlo techniques similar to those used before. Careful analysis of the data showed, however, that instead of phase separation there are independent small FM polarons. We have recently extended these studies to the two-dimensional case²⁹ for doping $0 < x \lesssim 12\%$ and at AFM corespin-coupling $J' = 0.02$. A thorough examination of a variety of observables showed that, like in 1D, there is no phase separation but holes enter the system by forming independent FM polarons with a single hole inside.

In the present paper we provide a phase diagram of the two-dimensional model as a function of corespin coupling J' and hole doping up to $x = 0.6$. We thoroughly examine the transition from the polaronic to the homogeneous ferromagnetic phase. At moderate to large J' the polarons persist, whereas at very small J' , phase separation occurs. In the homogeneous phase, strong FM order is only present at small to moderate J' .

At least for small doping, polarons are favored over

phase separation by entropy, and their dependence on temperature is therefore of interest. Previous studies have mostly employed an inverse temperature of $\beta = 50$ (corresponding to an experimentally relevant temperature of 50-100K, depending on hopping strength). We show that further lowering the temperature actually *strengthens* the polarons, even though the effect of entropy is reduced, i.e., they are also energetically favored. Only at small J' , low temperatures enhance a tendency to phase separation and toward diagonal chains of holes.

We also investigate the 3D model where we likewise find independent polarons at small doping, and in addition a 'polaron lattice' at higher doping. No phase separation is observed at any doping.

The outline of this paper is as follows. In Sec. II we introduce the Hamiltonian and the numerical method. In Sec. III we establish FM model polarons in two and three dimensions; we give an analytic estimate of their energy compared to phase separation in Sec. III A and find polarons to dominate except for very small J' . Section IV contains unbiased MC results for the two dimensional model. We present a phase diagram for $\beta = 50$ in Sec. IV D.

We study temperature effects in Sec. IV E, and a phase diagram for lower temperature $\beta = 80$ (30K – 60K) is presented in Sec. IV E 4.

Finally, we present unbiased MC data on the three dimensional model at $0 < x \lesssim 0.4$ in Sec. V.

II. MODEL HAMILTONIAN AND METHOD

In this paper, we treat the ferromagnetic Kondo lattice model in two and three dimensions with one orbital and classical corespins. We treat configurations with the electron spin antiparallel to the local corespin in second order perturbation theory, as proposed in Ref. 10, which is a systematic improvement over the $J_H \rightarrow \infty$ approach. The resulting effective spinless fermion (ESF) Hamiltonian is

$$\hat{H} = - \sum_{\langle i,j \rangle} t_{i,j}^{\uparrow\uparrow} c_i^\dagger c_j - \sum_{i,j} \frac{t_{i,j}^{\uparrow\downarrow} t_{j,i}^{\downarrow\uparrow}}{2J_H} c_i^\dagger c_i + J' \sum_{\langle i,j \rangle} \mathbf{S}_i \cdot \mathbf{S}_j. \quad (1)$$

The spinless fermion operator c_j (c_i^\dagger) destroys (creates) a *local* spin-up electron (i.e. an electron with spin parallel to the corespin at the same site) at site i . Down electrons have been integrated out, and the spin index has therefore been omitted. Since the local corespins may point in an arbitrary direction, the ESF model (1) still contains contributions from both spin orientations with respect to a *global* spin-quantization axis. J_H is the large ferromagnetic coupling of the e_g electron spin to the corespin and is set to $J_H = 6$ throughout this work. The small AFM superexchange parameter J' takes values between $J' = 0$ and $J' = 0.05$ for manganites.

The hopping strength $t_{i,j}^{\uparrow\uparrow}$ in the kinetic energy (first term of Eq.1) depends on the relative angle $\vartheta_{i,j}$ between

the corespins at the two neighboring sites:

$$t_{i,j}^{\uparrow\uparrow} = t_0 u_{i,j}^{\uparrow\uparrow} = t_0 (c_i c_j + s_i s_j e^{i(\phi_j - \phi_i)}) = t_0 \cos(\vartheta_{ij}/2) e^{i\vartheta_{ij}}, \quad (2)$$

where $c_i = \cos(\vartheta_i/2)$ and $s_i = \sin(\vartheta_i/2)$. The factor depends on the polar coordinates ϑ and ϕ of the corespins and contains a complex phase factor, which can lead among others to the so called ‘‘Flux Phase’’, see Refs. 19,30,31 and Sec. IV C. We use the parameter $t_0 = 1$ as unit of energy throughout this paper.

The second term in Eq. 1 contains the second order treatment of the virtual excitations, where an up-electron at site i can become a down-electron at site j and immediately hop back to become an up-electron at site i again. Its strength also depends on the corespins but is always real:

$$t_{i,j}^{\uparrow\downarrow} t_{j,i}^{\downarrow\uparrow} = t_0^2 |u_{i,j}^{\uparrow\downarrow}|^2 = t_0 (|c_i s_j e^{-i\phi_j} + s_i c_j e^{-i\phi_i}|^2) = t_0 \sin(\vartheta_{ij}/2)^2. \quad (3)$$

We treat this Hamiltonian by unbiased Monte Carlo simulations for the grand canonical ensemble using the standard algorithm⁵ and for the canonical ensemble with the algorithm proposed in Ref. 29. The lattice size is 12×14 sites in 2D and $6 \times 6 \times 4$ in 3D where not otherwise indicated. We mainly choose non-quadratic lattices in order to minimize finite size effects due to closed shells. For our MC results, 50 to 200 lattice sweeps have been skipped between measurements and autocorrelations have been analyzed. Wherever they are found to be very long (notably around the phase boundary between the Flux phase and the FM/PM phase and for the vertical stripe phase), parallel tempering^{32,33,34} has been employed.

III. FM MODEL-POLARONS IN 2D AND 3D

In Ref. 29, we showed that the results of unbiased Monte Carlo simulations for $J' = 0.02$, $\beta = 50$ and $J_H = 6$ for doping levels up to $x \approx 12\%$ (i.e. near the completely filled lower Kondo band) correspond to independent ferromagnetic polarons and not to phase separation. To this end, we constructed a model of independent polarons, evaluated several observables (spectral density, DOS, corespin correlation and dressed corespin correlation Eq. (6)) for this model, compared the results to the MC data and found almost perfect agreement.

In the undoped case $x = 0$, the corespins are aligned antiferromagnetically because of virtual excitations into the upper Kondo band and because of the AFM superexchange J' . The effective strength of the antiferromagnetic interaction is given by $J_{\text{eff}} = J' + \frac{1}{2J_H}$ for $n \approx 1$.¹⁰ One FM polaron in 2D consists of just one spin flipped from the AFM background and thus forming a five-site FM region where a hole is trapped, see Fig. 1(a). The eigenstates of the hole inside this small FM cluster lead to signals at $\omega = \pm 2$ and at $\omega = 0$ in the spectral density

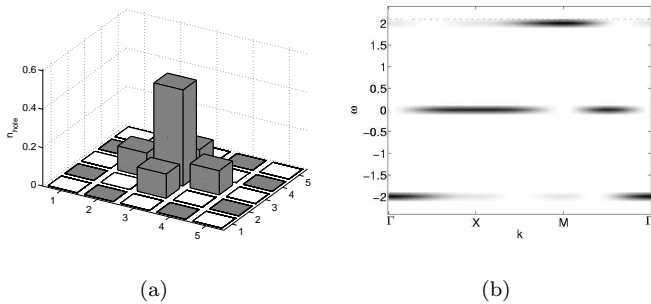


FIG. 1: Idealized two-dimensional FM polaron of $L_f = 5$ lattice sites, embedded in an AFM background (shown in Ref. 29) (a) Spin and hole-density configuration for the groundstate. Empty (filled) squares represent spin down (up). Height represents hole density. (b) Contribution of the polaron to the one-particle spectral function. For visibility, the δ -peaks in the spectral density have been broadened to a width of 0.2.

and the DOS, see Fig. 1(b). For a large number of polarons, i.e., of flipped spins, the FM polarons occasionally overlap and thereby form larger FM areas; such overlaps are neither suppressed nor encouraged in the independent polaron model.

In 3D, the situation is very similar: When one spin is flipped in the AFM lattice, a FM domain of seven sites results. This is schematically depicted in Fig. 2. Its eigenenergies are given by $\omega = 0$ (fourfold degenerate) and $\omega = \pm\sqrt{6}$. When a hole is inserted into the 3D lattice, it can gain the energy $-\sqrt{6}$, but the energy $12J_{\text{eff}}$ for the breaking of six AFM bonds has to be paid. The polaron energy is therefore given by

$$e_{\text{pol}} = -\sqrt{6} + 12 J_{\text{eff}}. \quad (4)$$

This energy determines the critical chemical potential $\mu^* = -e_{\text{pol}}$, at which holes that form polarons enter the completely filled lower Kondo band of a 3D system. Interestingly, such seven-site stars were also reported to result from combined lattice and spin effects for the electron doped system, i.e., for few electrons.³⁵

A. Energy comparison of Phase Separation and FM Polarons

We examine the competition of phase separation and FM polarons by comparing their energies for the relevant range of the effective antiferromagnetic superexchange $J_{\text{eff}} = J' + \frac{1}{2J_H}$, which can of course only be done approximately. We obtain the critical chemical potential μ_{PS} for phase separation by setting the energy of the completely filled AFM band equal to that of a partially

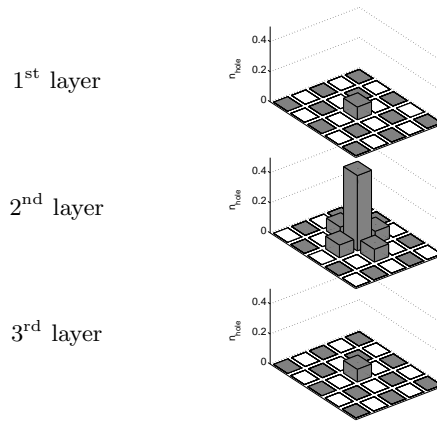


FIG. 2: Spin and hole-density configuration of an idealized three-dimensional FM polaron of $L_f = 7$ lattice sites, embedded in an AFM background. The three layers represent three consecutive plains in the 3D lattice. Empty (filled) squares represent spin down (up). Height represents hole density in the ground state.

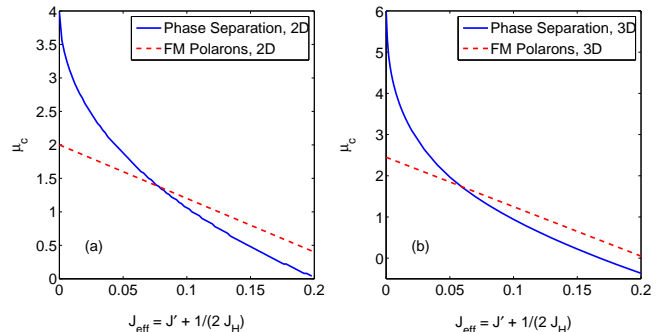


FIG. 3: (Color online) Critical chemical potential for phase separation (solid line) and FM polarons of the shape depicted in Fig. 1(a) for (a): 2 dimension and (b) 3 dimensions.

filled FM band.

$$-\mu_{\text{PS}} - zJ_{\text{eff}} \stackrel{!}{=} \underbrace{\int_{-z}^{\mu_{\text{PS}}} \epsilon n(\epsilon) d\epsilon}_{e_{\text{kin}}} - \mu_{\text{PS}} \int_{-z}^{\mu_{\text{PS}}} n(\epsilon) d\epsilon, \quad (5)$$

where z is the number of nearest neighbors for each site (4 in 2D, 6 in 3D) and $n(\epsilon)$ is the one-particle density of states of a tight binding band with $\epsilon(k_x, k_y) = -2 \cos(k_x) - 2 \cos(k_y)$ or $\epsilon(k_x, k_y, k_z) = -2 \cos(k_x) - 2 \cos(k_y) - 2 \cos(k_z)$, respectively. The kinetic energy per site e_{kin} (first term on the right-hand side) is zero for the completely filled band.

The critical chemical potential for FM polarons is given by $\mu_{\text{pol}} = 2 - 8J_{\text{eff}}$ in 2D (see Ref. 29) and $\mu_{\text{pol}} = \sqrt{6} - 12J_{\text{eff}}$ in 3D (see Eq.4). It is compared to μ_{PS} in Fig. 3 for two and three dimensions. In contrast to the energy minimization performed for 1D systems (given in Ref. 18)

we did not optimize the shape of the polarons, but we always used polarons consisting of one single flipped spin as depicted in Figs. 1(a) and 2. This puts FM polarons slightly at a disadvantage.

For μ larger than the critical values, the band is completely filled and AFM. When the chemical potential is lowered and holes are introduced into the system, this leads to PS if $\mu_{\text{PS}} > \mu_{\text{pol}}$ and to polarons if $\mu_{\text{pol}} > \mu_{\text{PS}}$.

For 2D, one sees that PS is favored for small $J_{\text{eff}} \lesssim 0.08$ in accordance with the MC data, see Sec. IV B. For the parameter $J_H = 6$ used in our calculations, $J_{\text{eff}} \approx 0.083$ corresponds to $J' = 0$, where we do indeed observe phase separation. For larger values of J_{eff} , i.e., smaller $J_H < 6$ or larger $J' > 0$, polarons are not only favored by entropy, but also by energy.

In three dimensions, the preference for polarons over PS sets in for even smaller values for J_{eff} .

IV. MC RESULTS FOR 2D

We first investigate the influence of AFM superexchange J' and doping x at $\beta = 50$, eventually leading to the phase diagram in Fig. 12. Temperature effects are discussed in Sec. IV E, with a phase diagram for $\beta = 80$ in Fig. 22.

A. $J' = 0.02$: From independent polarons to phase separation

In Ref. 29, we found a very close correspondence of the MC data with the results from the polaron model for all observables up to doping levels of $x \approx 12\%$, where the polarons already cover approximately 60% of the lattice. The polarons appear to be independent, with overlapping polarons occurring at a similar rate as for the independent polaron model.

In this section, we investigate higher doping levels $x > 12\%$ at $\beta = 50$, where the results begin to deviate from the independent polaron results; the homogeneous FM phase sets in at $x \approx 21\%$. In between, the polarons attract each other which leads to phase separation (PS). The transition from polarons to PS is not well defined. The polarons first coexist with large clusters, which finally dominate. This development is illustrated in the MC snapshots depicted in Fig. 4. It shows snapshots for 20 holes ($x \approx 12\%$), where 19 polarons can be seen and only one hole is delocalized, for 24 holes ($x \approx 14\%$), where polarons coexist with a larger and more homogeneous area, and finally for 31 holes ($x \approx 18.5\%$). This last doping is only approximately 4 holes away from the homogeneous FM phase at $x \gtrsim 21\%$, and even there, some polarons persist.

In order to check whether the addition of holes leads primarily to more small polarons or to a growth of the existing ones, we compute a dressed corespin correlation

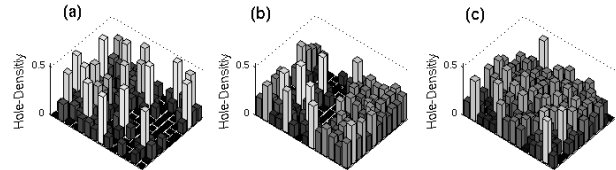


FIG. 4: MC snapshot of the hole density for (a) 20 holes ($x \approx 12\%$, shown in Ref. 29), (b) 24 ($x \approx 14\%$), and (c) 31 ($x \approx 18\%$) holes in a 14×12 lattice at $\beta = 50$, $J' = 0.02$, $J_H = 6$. Height represents hole density, grayshades are for better visibility.

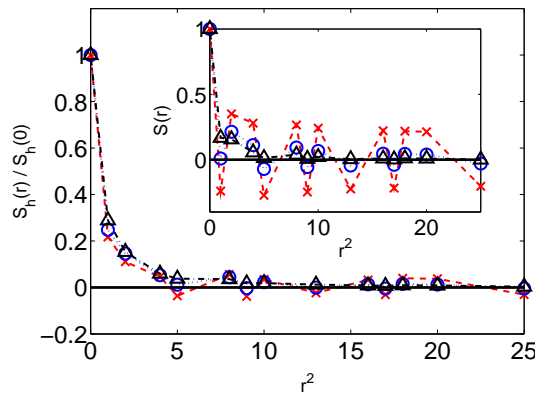


FIG. 5: (Color online) Dressed corespin correlation Eq. (6) for 24 holes (\times , dashed), 31 holes (\circ , dotted) and ≈ 36 (Δ , dash-dotted) holes. The inset shows the usual corespin correlation in real space $S(\vec{r}) = \frac{1}{L} \sum_{\vec{i}} S_{\vec{i}} S_{\vec{i}+\vec{r}}$. Remaining parameters as Fig. 4.

function

$$S_h(\vec{r}) = \frac{1}{L} \sum_{\vec{i}} n_{\vec{i}}^h S_{\vec{i}} S_{\vec{i}+\vec{r}}. \quad (6)$$

The hole density at site \vec{i} , denoted by $n_{\vec{i}}^h$, is related to the electron density via $n_{\vec{i}}^h = 1 - n_{\vec{i}} = 1 - \langle c_{\vec{i}}^\dagger c_{\vec{i}} \rangle_{\mathcal{S}}$, where $\langle n_{\vec{i}} \rangle_{\mathcal{S}}$ is the expectation value of the density given the corespin configuration \mathcal{S} . The sum over \vec{i} is taken over all lattice sites and the observable is averaged over all corespin configurations \mathcal{S} occurring in the MC run. The dressed correlation measures the ferromagnetic regions around holes.

Figure 5 shows $S_h(\vec{r})$ for 24, 31 and ≈ 36 holes. The latter doping marks the point, where the more homogeneous phase sets in and where the compressibility becomes much smaller than in the polaronic and phase separated regimes, so that this filling can be obtained in the grand canonical ensemble. One sees that the ferromagnetic regions around the holes grow slightly with doping, e. g., the correlation at $r^2 = 5$ goes from AFM to FM. This is an indication for phase separation. The usual

corespin correlation in real space is shown in the inset. It shows the evolution of short-range ferromagnetic correlations. However, no long-range FM correlations are present even for ≈ 36 holes ($x \approx 21\%$). This shows that the orientation of the small FM clusters is largely independent, see also the spin structure factor in Sec. IV C. We therefore do not have coexistence of macroscopic FM and AFM phases at any point for $J' = 0.02$.

B. Dependence of Polarons and Phase Separation on J'

Although J' is usually taken to be very small compared to the other parameters in the Hamiltonian, it has a considerable influence on the polaronic regime, because it stabilizes the AFM background.

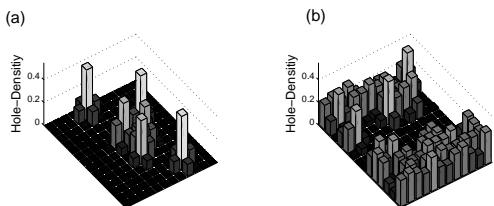


FIG. 6: Monte Carlo snapshots for $J' = 0$ and $\beta = 50$. (a) 6 holes, polarons; (b) 20 holes, phase separation. The MC simulations were done for $J_H = 6$, $\beta = 50$ on a 12×14 lattice. Height represents hole density, grayshades are for better visibility.

For $J' = 0$ and $\beta = 50$, MC snapshots shown in Fig. 6 reveal polarons with a tendency to form clusters for a few holes and phase separation for larger doping.

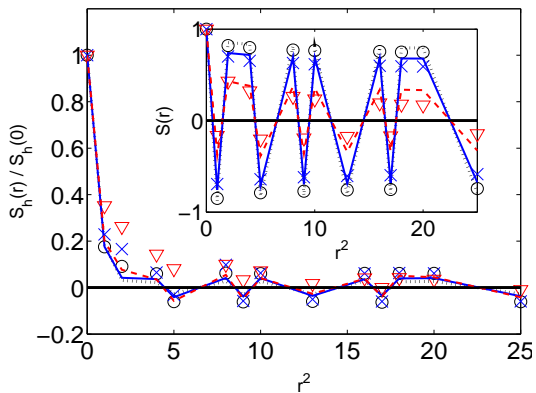


FIG. 7: (Color online) Dressed corespin correlation Eq. (6) from unbiased MC Data for $J' = 0$ (symbols) and $J' = 0.02$ (continuous lines) for 1 (\circ , dotted), 6 (\times , solid) and 20 (∇ , dashed) holes. The inset shows the corespin correlation. Parameters as in Fig. 6.

The dressed spin correlation Eq. (6) for 1, 6 and 20 holes is depicted in Fig. 7 for $J' = 0$ and $J' = 0.02$. In

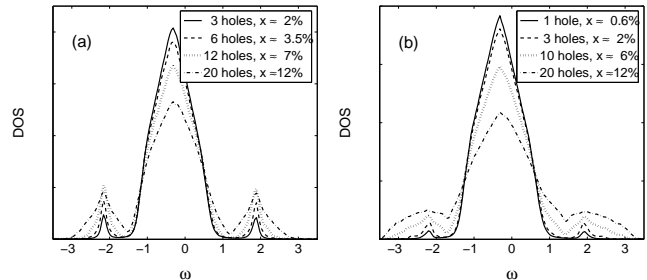


FIG. 8: One-particle DOS for (a) $J' = 0.02$ (shown in Ref. 29) and for (b) $J' = 0$, other parameters as in Fig. 6.

this doping range, the ferromagnetic regions around the holes do not grow with doping for $J' = 0.02$ (continuous lines), instead, the nearest AFM correlation at $r^2 = 5$ remains AFM, which indicates polarons. In contrast, the FM regions do grow for $J' = 0$ (symbols), this growth suggests larger FM regions, i.e. phase separation. Also, the antiferromagnetic correlations shown in the inset decrease faster for $J' = 0$ than for $J' = 0.02$.

Fig. 8 shows the DOS for $J' = 0.02$ and for $J' = 0$ at various fillings. For both values of J' and all depicted doping ranges, one sees the central band which stems from the movement of the electrons in the imperfect AFM background. This band is completely filled. For small doping, one sees the polaronic states at $\omega \approx \pm 2$, see also Fig. 1. For $J' = 0.02$, the weight of these peaks increases with doping, but their shape changes only for very large doping, in accordance with independent polaron results.²⁹ The pseudogap remains clearly visible. For $J' = 0$, one also sees the polaronic states and the pseudogap for small doping, but the pseudogap is filled at larger doping. The states filling the pseudogap stem from larger FM clusters, and these are larger and more frequent than can be accounted for by occasionally overlapping independent polarons. The actual experimental observation of the pseudogap^{36,37,38,39} rather favors the polaron scenario as opposed to PS.

Figure 9 shows the spectral density for $J' = 0$, $J' = 0.02$, and $J' = 0.05$ for 20 or 21 holes, i.e. $x \approx 12\%$. The larger FM areas for $J' = 0$ [top panel (a)] lead to a second band in addition to the one stemming from the AFM parts of the lattice. It has a larger bandwidth, because the corespin correlations are ferromagnetic and the hopping strength is therefore larger. The central panel (b) shows the results for the independent polarons at $J' = 0.02$ (also given in Ref. 29). Around the polaronic states at $\omega = \pm 2$, one sees the signals from overlapping polarons, which are also there for the independent polaron model.²⁹ The signals from the small FM clusters do not form a continuous band, but are instead separated from the AFM band by the pseudogap.

A stronger antiferromagnetic superexchange $J' = 0.05$ suppresses configurations with overlapping polarons, as

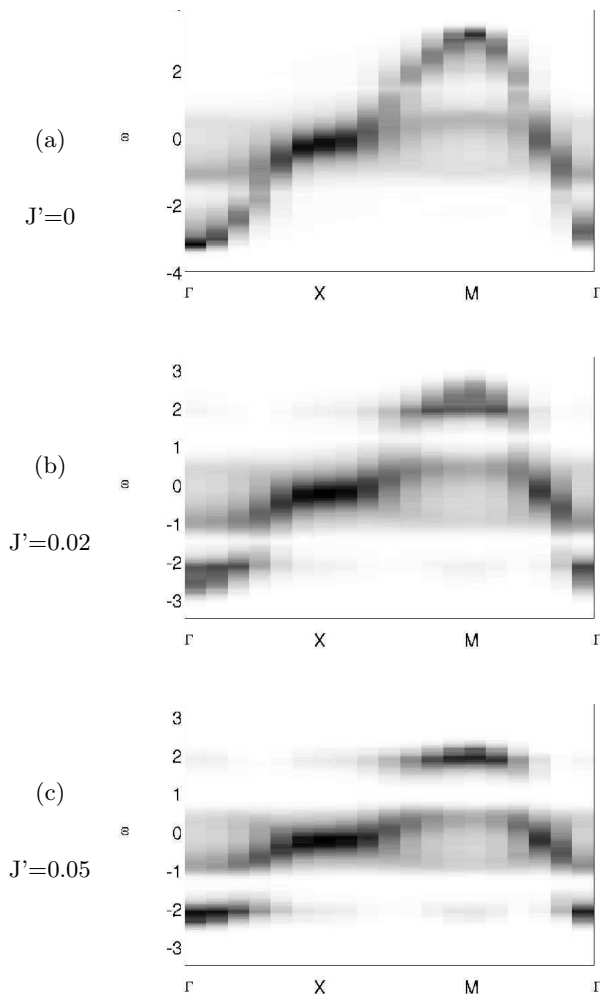


FIG. 9: Spectral density for $x \approx 12\%$ and (a) $J' = 0$ (20 holes), (b) $J' = 0.02$ (20 holes, also shown in Ref. 29), and (c) $J' = 0.05$ (21 holes) on a 12×14 lattice, $\beta = 50$, $J_H = 6$.

can be seen in the lowest panel, Fig. 9(c). In addition to the antiferromagnet, the data for $J' = 0.05$ show almost only one-polaron states and the pseudogap is more pronounced. This shows that not even overlapping polarons exist for $J' = 0.05$, let alone phase separation. The reason for this behavior is that larger J' favors antiferromagnetically stacked polarons over larger clusters. This can be seen in another dressed corespin correlation, which takes into account hole densities at both lattice sites:

$$S_{hh}(\vec{r}) = \frac{1}{L} \sum_{\vec{i}} n_i^h S_i^h n_{i+\vec{r}}^h S_{i+\vec{r}}^h. \quad (7)$$

Note that even without the corespins, this would *not* give the usual density correlation, because it measures $n_i n_j = \langle c_i^\dagger c_i \rangle_S \langle c_j^\dagger c_j \rangle_S$ instead of $\langle c_i^\dagger c_i c_j^\dagger c_j \rangle_S$. Eventually, this observable is of course averaged over all spin

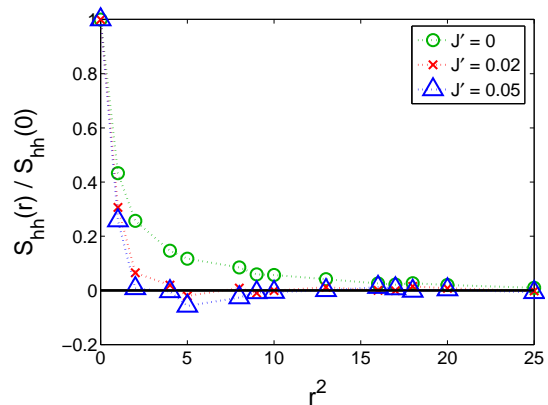


FIG. 10: (Color online) Hole-spin-hole-spin correlation as defined in Eq.7 for 20 holes and various values of J' : Other parameters as in Fig. 6

configurations \mathcal{S} obtained in the Monte Carlo run. This correlation is depicted in Fig. 10 for 20 holes ($x \approx 12\%$) and for $J' = 0$, $J' = 0.02$ and $J' = 0.05$. One sees a positive correlation indicating PS for $J' = 0$, almost only short-range correlations over two sites (one polaron) for $J' = 0.02$ and a negative correlation at $r^2 = 5$ for $J' = 0.05$, which indicates antiferromagnetically stacked neighboring polarons.

C. FM, PM and Flux Phase

The exchange interaction also plays an important role at electron densities below the polaronic and phase separated regimes, i. e., at larger doping levels $x \gtrsim 0.2$, which corresponds to chemical potentials $\mu < \mu^* = -\epsilon_{\text{pol}}$.

For small to medium $J' \lesssim 0.03$, this region is ferromagnetic because of the dominant double-exchange. The corespin structure factor $S(\vec{k})$ is depicted in fig. 11 for $J' = 0.02$ and variable filling. The curve for $x \approx 12\%$, which is in the polaronic regime, shows a clear AFM signal. There is a barely visible FM signal, but it is very small in spite of the rather large doping, because the polarons are independent and not mutually aligned. Just below μ^* , corresponding to $x \approx 21\%$, the AFM peak has almost vanished and there is a slightly larger FM peak at $(0,0)$. This means that the ferromagnetism is not very strong and that even some remnant of the AFM remains, see also the corespin correlation in real space in Fig. 5. The lattice is however homogeneous and the spectral density (not shown) consists of one single tight binding band with reduced hopping strength $t \approx 0.75$ and with broadened signals. For larger doping $x \approx 29\%$ and $x \approx 32\%$, the spin structure factor $S(\vec{k})$ shows that the ferromagnetism grows upon increasing the hole density up towards half-filling of the lower Kondo band. The bandwidth then increases and the signals in the spectral density become sharper, as fluctuations of the corespins are suppressed by the kinetic energy.

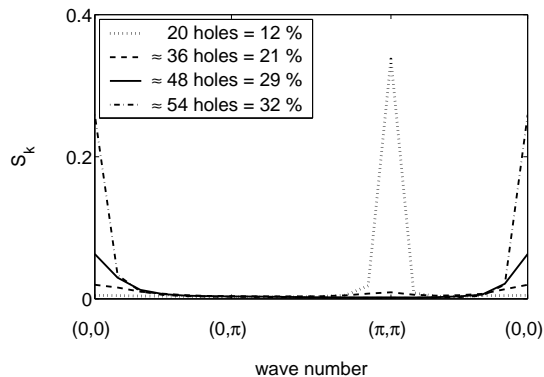


FIG. 11: Spin-spin correlation in momentum space for various hole doping, $J' = 0.02$, $J_H = 6$ and $\beta = 50$.

With increasing J' , however, the ferromagnetism gradually becomes weaker and for $J' = 0.05$, $S(\vec{k})$ does not show any signal at $(0, 0)$ for any doping $x < 0.5$. Instead, the so called “Flux phase” appears around half filling. The band structure then has a pseudogap at half-filling and differs markedly from the tight-binding-DOS of a ferromagnetic or paramagnetic lattice. The spin structure factor shows signals at $(0, \pi)$ and $(\pi, 0)$.^{19,30,31,40}

D. Phase Diagram for $\beta = 50$

In order to determine the phase diagram, shown in Fig. 12, criteria to distinguish the phases have to be specified. For the crossover from the polaronic to the phase separated regime, we choose the filling, at which the ferromagnetic regions around the holes - detected by dressed corespin correlation Eq. (6) - begin to extend, i. e., when the nearest antiferromagnetic correlations at $r^2 = 5$ become ferromagnetic. It must be emphasized that the transition is a gradual one: larger ferromagnetic domains occasionally occur at smaller doping and above all polarons persist to larger doping (Sec. IV A). This criterion is therefore somewhat arbitrary.

To determine the phase boundary between the polaronic/phase separated region and ferromagnetism on one hand, and between the polaronic regime and paramagnetism on the other, we choose the electron density just below the discontinuity at the critical μ^* , although the antiferromagnetic peak may still be visible at this point; the distinction is therefore rather based on the compressibility. From there on, a system is labeled “ferromagnetic” or “paramagnetic”.

In the paramagnetic regime, we find hardly any magnetic structure for intermediate doping, until the signals from the Flux phase begin to appear. The crossover from FM to PM is continuous and depends on doping, larger x leading to more ferromagnetism. As a criterion for the transition from FM to Flux phase, one can take the maximal change of the corespin moment with filling $d|S_{\text{tot}}|/dN$, because $|S_{\text{tot}}| = 0$ for the ideal Flux phase.

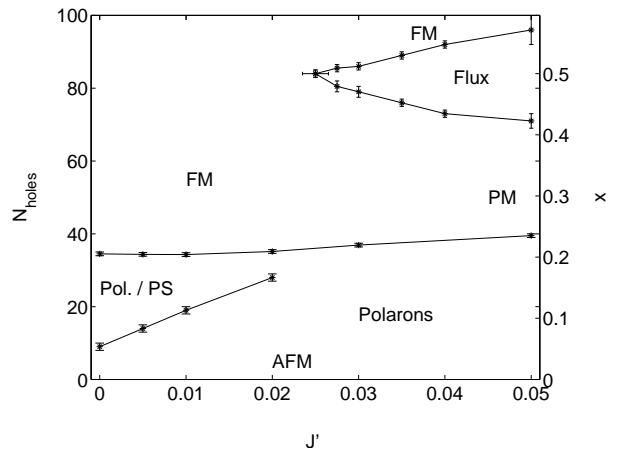


FIG. 12: Phase diagram for $J_H = 6$, $\beta = 50$, $0 \leq J' \leq 0.05$ and $0 \leq x \leq 0.6$ (i.e. filled to 40% filled lower Kondo band) on a 14×12 -lattice. “Pol.”: polaronic regime, “Pol./PS”: mixture of both polarons and larger ferromagnetic clusters, “AFM”: antiferromagnet, “FM”: ferromagnet, “PM”: regime without magnetic structure, “Flux”: Flux phase.

Obviously, this becomes less exact as the ferromagnetism is weakened. A further indicator is the change in the spectral density, which for the Flux phase differs very much from a tight-binding one. The Flux phase is subject to strong finite size effects, which are caused by the fact that only a very small part of the Brillouin zone contributes to the few states around the pseudogap around $(\pi/2, \pi/2)$. For this reason, lattices of different sizes, above all square systems because of closed shell effects, may exhibit the transition from ferro-/paramagnetism to the Flux phase at slightly different filling. For hole dopings above the Flux phase, all systems become ferromagnetic.

The resulting phase diagram with the phases discussed above is shown in Fig. 12.

E. Effects of a lower temperature

1. $J' = 0.02$: Polarons stabilized further

For $J' = 0.02$, where the system can be well described by independent polarons at $\beta = 50$ and $x \lesssim 12\%$, cooling to $\beta = 80$ suppresses overlapping polarons, larger ferromagnetic regions and phase separation. The suppression of overlapping polarons can, e.g., be seen by comparing the spectral density at doping $x = 12\%$ (20 holes) for $J' = 0.02$ and $\beta = 80$ (Fig. 13) to the one for $\beta = 50$ (Fig. 9(b)). Besides the narrowed antiferromagnetic band, almost only one polaron signals are seen at the lower temperature, which means that the polarons are not independent but avoid overlapping.

The suppression of phase separation by lower temperature is clearly visible in the MC snapshots for 28 holes ($x \approx 17\%$) depicted in Fig. 14. While only a few polarons

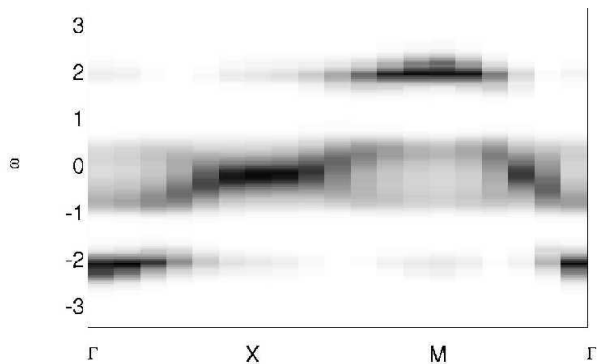


FIG. 13: Spectral density (same as fig. 9(b), but for lower temperature $\beta = 80$.)

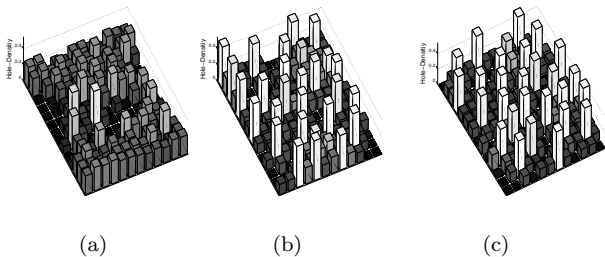


FIG. 14: MC snapshot of the hole density for 28 holes ($x \approx 17\%$) at temperatures (a) $\beta = 50$, (b) $\beta = 80$, (c) and $\beta = 100$. Other parameters as in Fig. 4.

exist for $\beta = 50$, they dominate at $\beta = 80$, where only a few holes are delocalized, and even more so at $\beta = 100$, where two polarons hardly ever share a site.

As for $\beta = 50$ and $J' = 0.05$, the reason for the polarons' dominance over PS is their antiferromagnetic stacking. Since each polaron takes 5 lattice sites, they can obviously no longer be stacked in this way for dopings larger than 20%. As can be seen in the phase diagram in Fig. 22, this doping is the point, where the larger clusters begin to dominate. In this case, the polaronic phase is more ordered than a phase separated scenario because of the stacking, and PS therefore occurs at higher temperature because of its higher entropy.

The stacking can be seen in the Hole-Spin-Hole-Spin correlation depicted in Fig. 15 for various doping levels. While one sees only short range correlations for 6 holes ($x = 3.5\%$), the antiferromagnetic stacking can be clearly observed for 28 holes ($x = 17\%$). This order disappears again for 34 holes ($x = 20\%$), when the polarons begin to merge. At this point, some tendencies to diagonal chains (see below) may exist at very low temperatures ($\beta = 100$).

In the ferromagnetic part of the phase diagram, a spin canted phase becomes actually more stable than ferromagnetism for some electron fillings and for periodic boundary conditions. Its spin structure factor has a peak for the smallest reciprocal lattice-vector of the system

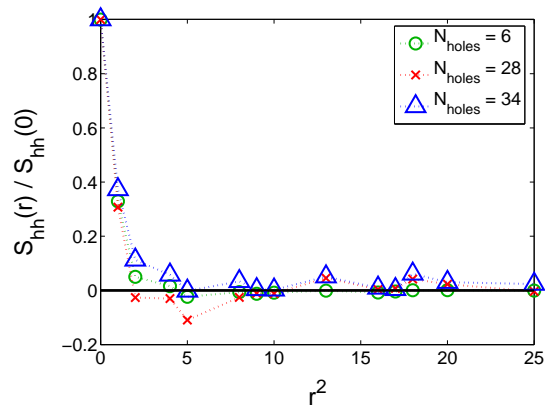


FIG. 15: (Color online) Hole-Spin-Hole-Spin correlation Eq.7 for $J' = 0.02$, $\beta = 80$ and various fillings. Other parameters as in Fig. 7

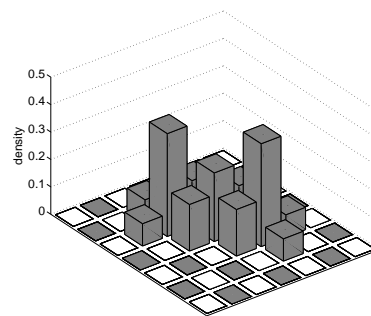


FIG. 16: Corespin configuration with three flipped spins, filled with two holes. Details as Fig. 1(a).

($\pi/7$ for a 14×12 lattice). Analytic energy comparison of the FM and this canted phase shows that the range of fillings, where the canted phase has lower energy, becomes smaller for larger lattices. Moreover, it is not present for open boundary conditions and thus probably a finite size effect. It shows, however, that ferromagnetism is not very dominant for doping levels near the phase separated regime.

2. $J' = 0$: Tendency to diagonal stripes

In Ref. 29, we showed that larger FM clusters with two flipped spins and two holes have (slightly) higher energy than two separated polarons. Fig. 16 depicts another possibility with three flipped spins but only two holes. The total kinetic energy of the two holes is then $0.61 t_0$ lower than that for two independent polarons. However, 3 spins have to be flipped instead of two, which costs the energy $8 \times J_{\text{eff}}$. The gain and the loss balance each other for $J_{\text{eff}} \approx 0.077$ in this simple model calculation. In the MC simulations, we observe tendencies to such configurations for $J' = 0$ ($J_{\text{eff}} \approx 0.083$), which extend to diagonal chains at higher doping, see the snapshots in Fig. 6. For larger hole doping, isotropic clusters coexist with these

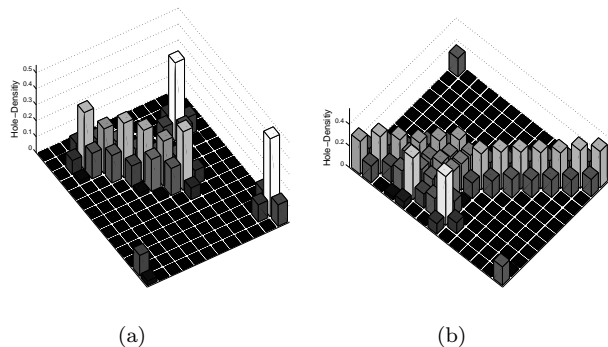


FIG. 17: Monte Carlo snapshots for $J' = 0.0$ and $\beta = 80$ and (a) 6 holes ($x \approx 4\%$), (b) 12 holes ($x \approx 7\%$). Height represents hole density, grayshades are for better visibility.

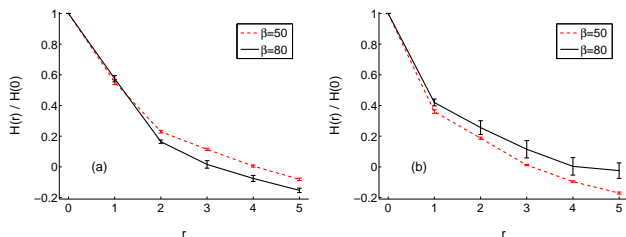


FIG. 18: (Color online) Hole correlation Eq. (8) for $J' = 0.0$ and 12 holes ($x = 7.1\%$): The left panel (a) shows the correlations in $(1,0)$ -direction; the right panel (b) shows the same for the diagonal $(1,1)$ -direction. Dashed line: $\beta = 50$, solid: $\beta = 80$.

diagonal chains and finally dominate. In order to measure these diagonal chains, we use the hole-correlation function

$$H(\vec{r}) = \frac{1}{L} \sum_{\vec{i}} (n_{\vec{i}}^h - \bar{n}_h) (n_{\vec{i}+\vec{r}}^h - \bar{n}_h), \quad (8)$$

where $n_{\vec{i}}^h$ is the expectation value of the hole density at site \vec{i} for a given corespin configuration and \bar{n}_h is the overall hole density. As explained for Eq. 7, this is not the usual density correlation function. The results for 12 holes ($x = 7.1\%$) are depicted in Fig. 18 and show that diagonal correlations are slightly enhanced at $\beta = 80$.

3. $J' = 0.05$: Vertical stripes

For $J' = 0.05$ and doping $x = 0.25$, low temperatures favor a stripe-phase with a periodicity of 4 sites perpendicular to the stripes. The spin configuration is schematically depicted in Fig. 19(a). The corespins are drawn within the xy -plane for visibility, but such configurations are not preferred over others with the corespins

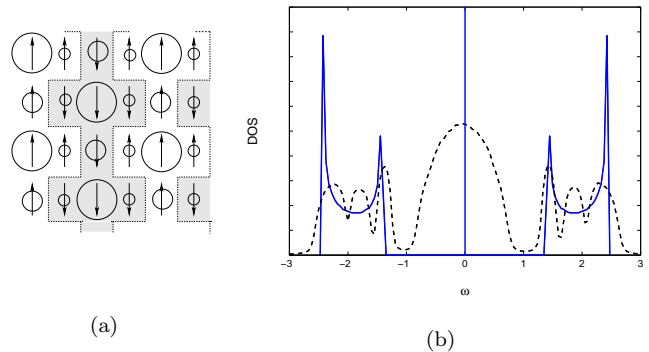


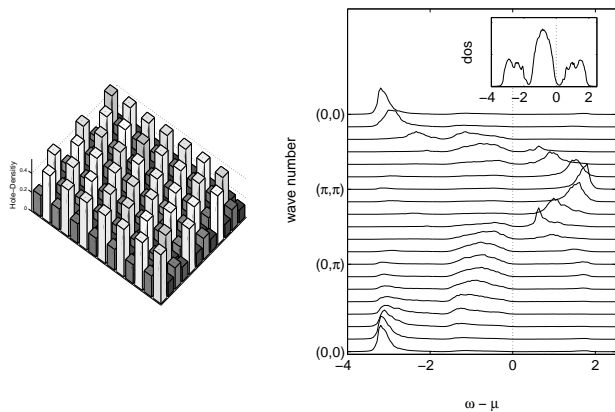
FIG. 19: (Color online) Stripe Phase for $J' = 0.05$ and $x = 0.25$. Left: Schematic representation of the corespins. The circles represent the holes density, but only qualitatively. Right: one-particle density of states of the two dispersive bands for $J_H \rightarrow \infty$ and the thermodynamic limit (continuous line) and for finite J_H on a 12×14 lattice with random fluctuations added to the corespins.

perpendicular to the plane of the 2D-lattice, because the Hamiltonian only depends on the relative orientation of neighboring spins, and a global rotation therefore has no effect.

For the schematic corespin configuration with perfectly aligned spins and with the approximation $J_H \rightarrow \infty$, the band structure is gapped and consists of several dispersionless bands at $\omega = 0$ and two bands with $\epsilon(k_x) = \pm \sqrt{4 \cos^2(k_x) + 2}$, when the stripes run in x -direction. As no hopping is possible between the antiparallel stripes, the band does not depend on the momentum perpendicular to the stripes. The resulting one-particle density of states for $J_H \rightarrow \infty$ and the thermodynamic limit can be seen in Fig. 19(b) (continuous line) and it is very similar to the DOS of one-dimensional tight-binding bands. For comparison to the MC data (inset of Fig. 20(b)), we also calculated the spectral density for finite J_H on a 12×14 lattice for the model corespin configuration with slight additional fluctuations (dashed line in Fig. 19(b)). The fluctuations were chosen so as to yield approximately the same width for the central band as the MC data. On a 24×12 lattice, the stripes can only develop in one direction, because 14 is not divisible by 4. One therefore can see the dependence of these bands on only one direction of the momentum quite clearly in the averaged spectral density depicted in Fig. 20(b). Fig. 20(a) shows an MC snapshot of this phase, where one sees stripes in the hole density.

Figure 21 shows the Hole-Spin-Hole-Spin correlation function Eq.7 for $x = 0.25$: One clearly sees the regular array of holes and the stripes in the corespins as depicted in Fig. 19(a).

The compressibility around this filling is very large, i.e., there is a jump in the electron density versus the chemical potential from $x \approx 0.29$ to $x \approx 0.23$ and the filling $x = 0.25$ can not be stabilized in the grand canonical



(a)

(b)

FIG. 20: MC snapshot and spectral density for $J' = 0.05$, $\beta = 80$, and $x = 0.25$. Left: MC snapshot: The heights represent hole densities, grayshades indicate FM (white) and AFM (black) correlations to the nearest neighbors. Right: Spectral density and one-particle DOS.

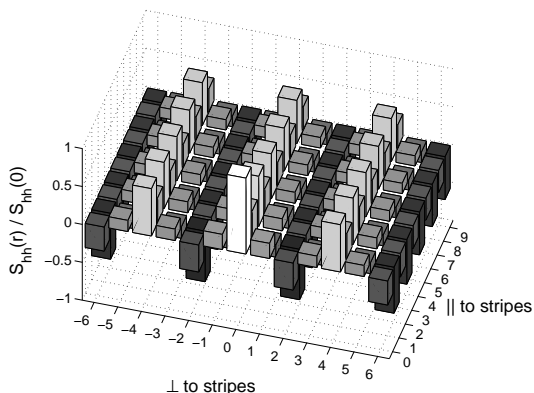


FIG. 21: Hole-Spin-Hole-Spin correlation Eq.7 for $J' = 0.05$, $\beta = 80$ and $x = 0.25$ (42 holes). Grayshades for better visibility.

ensemble. The discontinuity is not present for the higher temperature $\beta = 50$, where there is no stripe phase. At fillings slightly away from $x = 0.25$, stripes develop in parts of the lattice and are mixed with polarons or larger clusters.

The occurrence of this stripe phase at $x = 0.25$ and $J' = 0.05$ is in contrast to the results reported by Aliaga *et al.*¹⁹, who found an island phase of antiferromagnetically stacked FM clusters of size 2 by 2 for this filling. The electron density is homogeneous in this phase, and every spin has two FM and two AFM neighbors. Their calculations were done for the $J_H \rightarrow \infty$ model, but with a larger J' , so as to give approximately the same effective parameter J_{eff} . This island phase can however not be stable on a 12×14 lattice. In order to check the validity

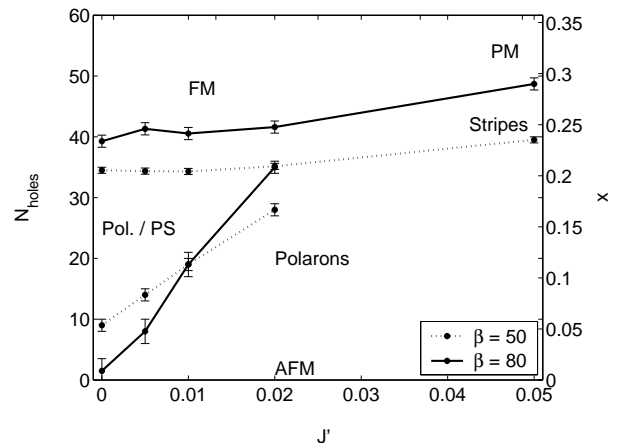


FIG. 22: Phase diagram for $\beta = 80$ and $\beta = 50$. Similar as fig. 12, but for a smaller range of doping. Solid lines: results for $\beta = 80$, dashed lines: $\beta = 50$.

of our results, we therefore repeated the simulations on a 12×12 system and still found stripes. Numeric comparison of the ground-state energies for perfect stripe and perfect island phase on a 12×12 lattice gave a lower energy for stripes for $J_H = 6$ and $J' = 0.05$ (corresponding to $J_{\text{eff}} \approx 0.133$ for $x = 0$ and to $J_{\text{eff}} \approx 0.1125$ for $x = 0.25$), but favored the island phase for $J_H = \infty$ and $J' = 0.133$ or $J' = 0.1125$. The reason lies in the density dependence of the AFM coupling coming from the virtual excitations (second term in Eq. 1), because the sites with 3 AFM and only one FM neighbor have high electron density and therefore maximize the gain from this interaction, whereas the holes weaken the interaction on the sites with predominately FM neighbors. This therefore presents a feature which is missing from the first order $J_H \rightarrow \infty$ approximation but is included in the second order approach to the FM Kondo model.

4. Phase diagram at $\beta = 80$

Our findings are summarized in the phase diagram for $\beta = 80$, $0 < x \leq 0.36$ and $0 \leq J' \leq 0.05$ depicted in Fig. 22. It shows that lower temperatures lead to larger clusters and PS for small $J' < 0.01$, while they favor individual polarons for more realistic values $J' > 0.01$. For the lower temperature, the homogeneous ferro-/paramagnetic phase only sets in at higher doping.

V. MC RESULTS FOR 3D

In three dimensions, we use a lattice of $6 \times 6 \times 4$ sites with periodic boundary conditions. For selected doping levels, we have repeated the simulations on lattices of different size in order to control finite size effects. As in one and two dimensions, the corespins are antiferromagnetically aligned for the filled lower Kondo band and the sys-

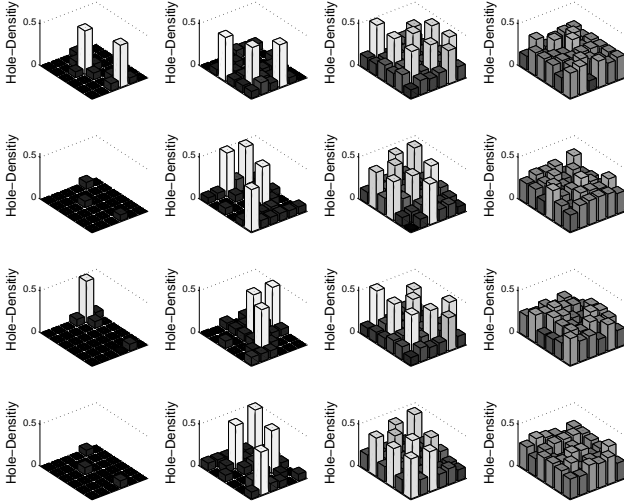


FIG. 23: MC snapshots for (a) 3 holes ($x \approx 2\%$), (b) 14 holes ($x \approx 10\%$), (c) 32 holes ($x \approx 22\%$) and (d) ≈ 38 holes ($x \approx 26\%$). The four plots stacked one above the other represent the 4 layers of the $6 \times 6 \times 4$ lattice, height represents hole density, grayshades are for better visibility. $J_H = 6, \beta = 50, J' = 0.02$.

tem exhibits a transition to ferromagnetism upon doping. Figure 23 shows MC snapshots for $J' = 0.02$ and $\beta = 50$ at various doping levels. For three holes ($x \approx 2\%$), one clearly sees three polarons of 7 sites each. The polarons also remain well separated for 14 holes ($x \approx 10\%$), although they take up $\approx 68\%$ of the lattice at this doping level. As every polaron contains 7 sites, no more than $x \approx 14\%$ holes can be doped into the lattice in this way. For the larger doping level $x \approx 22\%$ (32 holes), one sees tendencies toward a superstructure of regularly arrayed holes, see Fig. 23(c), which we termed ‘polaron lattice’. An idealized representation of the polaron lattice is depicted in figure 24, which is for a doping concentration of $x = 0.25$. The idealized version consists of two sublattices with opposing corespin and hole density is high on sites with four FM neighbors. Interestingly, at this ‘optimal’ doping concentration for the polaron lattice, the actual MC simulations favor a more homogeneous and disordered structure, like the one depicted in Fig. 23(d), which has been obtained for $x \approx 27\%$ (≈ 39 holes).

On very small systems ($4 \times 4 \times 4$ and $4 \times 4 \times 6$), the polaron lattice competes with a three-dimensional form of the vertical stripes found in 2D for $J' = 0.05$ and $\beta = 80$ (Sec. IVE3). Due to their periodicity, the stripes can only develop on lattices, where at least two of the three dimensions are divisible by four, and they do therefore not occur on a $6 \times 6 \times 4$ -system. Numeric comparison of the energies of the polaron lattice and the stripe-structure for $x = 0.25$ on systems of different size revealed that the polaron lattice has lower energy for systems which are larger than 4 in at least two directions, i.e., for lattices which are not of the shape $4 \times 4 \times L_z$.

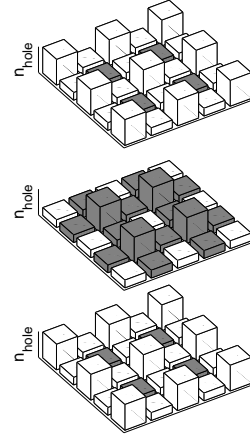


FIG. 24: Schematic representation of the corespins and density for the ‘polaron lattice’. Empty(filled) spins denote spin up(down), height represents hole density.

In order to verify this result, we performed Monte Carlo simulations on an $8 \times 6 \times 4$ -system and indeed found a polaron lattice.

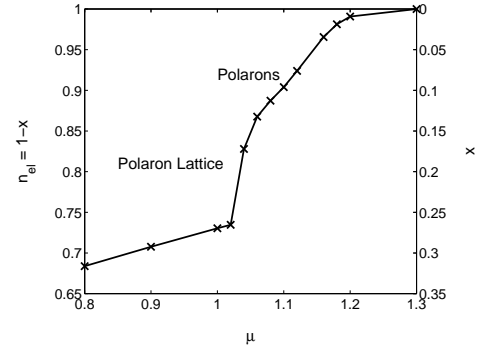


FIG. 25: Electron density $n_{el} = 1 - x$ vs. chemical potential μ in 3D. Parameters as Fig. 23.

The dependence of the electron density on the chemical potential is given in Fig. 25. The slope of the curve n_{el} vs. μ (i.e. the compressibility) is finite for the polaronic phase near $n_{el} = 1$ in contrast to the results for independent polarons,^{18,29} because the polarons avoid overlapping and it therefore becomes harder to fit more holes into the lattice. At $x \approx 1/7$ ($n_{el} \approx 0.86$), when there is no more room for polarons, the situation changes. The slope of n_{el} vs. μ becomes steeper, and the polaron lattice partially develops until $x \lesssim 23\%$, where the homogeneous disordered phase sets in. At $x \approx 27\%$, the compressibility is suddenly much reduced. It is not clear, why the homogeneous phase has such a high compressibility for $0.23 < x < 0.27$, and this may be a finite size effect. The lattice is not phase separated in this regime, snapshots are similar to the one depicted in Fig. 23(d), with some sites (scattered throughout the lattice) having

much higher or lower density than others. After ferromagnetism has become established at still higher doping values ($x \gtrsim 30\%$), the density becomes more evenly distributed (not shown).

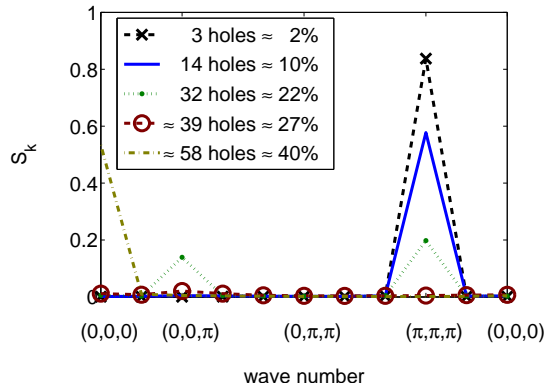


FIG. 26: (Color online) 3d Corespin Structure Factor for various doping levels. Parameters as Fig. 23

Figure 26 shows the momentum dependent corespin correlations for approximately the same dopings as the snapshots. For the almost filled band (3 holes, $x \approx 2\%$), it shows antiferromagnetism which decreases slightly for 14 holes ($x \approx 10\%$). For 32 holes ($x \approx 22\%$), the partial polaron lattice, a second peak appears for $k = (0, 0, \pi)$. For the polaron lattice, according to figure 24, the majority spin for consecutive planes alternates, which explains the signal at $(0, 0, \pi)$ in $S(\vec{k})$. The corespin structure is isotropic, the same alternating structure occurs in x - and y - direction and analogous signals appear at $(0, \pi, 0)$ and $(\pi, 0, 0)$. For the more homogeneous phase at ≈ 39 holes there is no magnetic structure, and ferromagnetism only begins to set in for ≈ 45 holes ($x \approx 30\%$, not shown) and it is established for ≈ 58 holes ($x \approx 40\%$).

Figure 27 shows the one-particle density of states for various doping levels. For 3 holes ($x \approx 2\%$), one sees the broadened central band from the AFM background and the signals from the polaronic states at $\omega \pm \sqrt{6}$. For 14 holes ($x \approx 10\%$), these signals are stronger and somewhat broader, because the polarons now cover a large part of the lattice and occasionally connect. For 32 holes ($x \approx 22\%$), the polaronic states have a considerable width, but the pseudogap is well preserved. In will be shown later, that these bands are the dispersive bands of the ‘polaron lattice’. The pseudogap has closed after the onset of the homogeneous phase at ≈ 39 holes ($x \approx 27\%$), but some remnant of it is still visible. For still higher doping of ≈ 58 holes ($x \approx 40\%$), where the lattice is ferromagnetic, the band (not shown) is a tight-binding band with a slightly reduced hopping amplitude.

In closing, let us discuss band structure and DOS for the ideal polaron lattice, depicted in figure 24. The unit cell in this case contains eight sites, and for perfectly FM/AFM corespins, the one-particle DOS has a degenerate non-dispersive band at $\omega = -2/J_H$ and two mo-

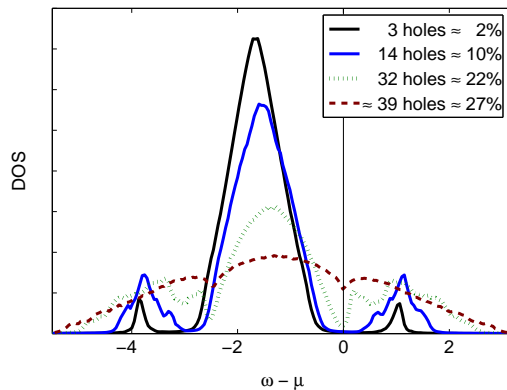


FIG. 27: (Color online) One-particle DOS for various doping levels. Parameters as in Fig. 23

mentum dependent bands at energies

$$\epsilon(k_x, k_y, k_z) = -\frac{1}{J_H} \pm \sqrt{\frac{1}{J_H^2} + 4(\cos^2(k_x) + \cos^2(k_y) + \cos^2(k_z))}. \quad (9)$$

The one-particle density of states resulting from this dispersion is depicted in Fig. 28 for a $6 \times 6 \times 4$ lattice (dash-dotted line). The two dispersive bands consist of a number of peaks because of finite size effects. For an infinite lattice (solid line), the DOS has a pseudogap between the dispersive bands and the central δ -peak. In addition, we have performed a model calculation, in which the corespins of the ideal polaron lattice are randomly disturbed. The DOS of the resulting tight-binding model with transfer integrals given by Eq. 2 is compared to the result of the ideal polaron lattice in Fig. 28. The amount of fluctuations has been chosen so as to give approximately the same width for the central band as the MC data (similar to Fig. 19(b)).

While the model calculation (for $x = 0.25$) differs slightly from the MC data for 32 holes ($x \approx 22\%$) depicted in Fig. 27, the width of the bands and their apparent double-peak structure is reproduced. The remaining differences are probably due to the fact that the MC data are for $x = 0.22$ and the polaron lattice is only partially developed, see the MC snapshot Fig. 23(c).

For $J' = 0$, diagonally arranged polarons similar to those observed in 2D (Sec. IVE2) were found for $x \lesssim 0.25$ on a $6 \times 6 \times 4$ lattice. These stripes occurred on every second plane along the z -direction (with $L_z = 4$). However, this phase was *not* observed on a $6 \times 6 \times 6$ lattice and we therefore consider it a finite size effect. On this larger lattice, we observed the ‘polaron lattice’ instead and the results were generally very similar to those for $J' = 0.02$.

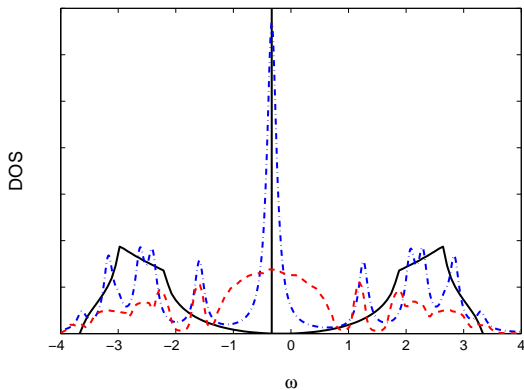


FIG. 28: (Color online) One particle DOS for the ideal polaron lattice in the thermodynamic limit (solid), for the ideal case on a $6 \times 6 \times 4$ lattice (dash-dotted line), and for $6 \times 6 \times 4$ with random fluctuations around the perfect spin arrangement (dashed line).

VI. CONCLUSIONS

We have used Monte Carlo simulations to examine the two- and three-dimensional ferromagnetic Kondo lattice model at small to medium hole doping and for parameters relevant to manganites. In three dimensions, we find that a small additional antiferromagnetic exchange $J' = 0.02$ yields very similar results as $J' = 0$. No phase separation is observed at any doping level. Instead, there are again polarons consisting of a single flipped spin in an AFM background and containing a single hole, which form a regular ‘polaron lattice’ when they become very dense.

In two dimensions, we have focused on the polaronic phase and its boundaries toward phase separation. At small hole doping, we find polarons for all values of the superexchange J' . For larger doping and small J' , e.g.,

$J' = 0$ instead of $J' = 0.02$, the polarons attract each other and tend to form larger clusters. Eventually, upon higher hole doping, phase separation into large ferromagnetic and antiferromagnetic regions sets in. A large antiferromagnetic superexchange ($J' = 0.05$), on the other hand, suppresses overlapping polarons and larger ferromagnetic regions, because it stabilizes the AFM background and favors antiferromagnetic stacking of the individual polarons. In the doping range $0.2 \lesssim x < 0.5$, J' suppresses the FM long-range order, so that the system is in reality rather paramagnetic than ferromagnetic for $J' \gtrsim 0.03$.

We find that lowering the temperature generally moves the homogeneous ferro-/para-magnetic phase to higher doping. Phase diagrams for $\beta = 50$ and $\beta = 80$ are given in Fig. 12 and Fig. 22. A lower temperature stabilizes the polarons and disfavors larger clusters for intermediate and large $J' \gtrsim 0.01$; for $J' = 0.02$, phase separation only occurs, when no more polarons can be fit into the lattice. PS is favored by lower temperatures only for unphysically small $J' \lesssim 0.01$. This is corroborated by a comparison of ground-state energies for idealized phase separation and polaron scenarios, which gives phase separation for small $J_{\text{eff}} \lesssim 0.08$ (corresponding to $J' \approx 0$ for $J_H = 6$), and polarons for larger $J_{\text{eff}} \gtrsim 0.08$. For $J' \approx 0$, lower temperatures enhance ferromagnetic diagonal chains with delocalized holes, while they lead to vertical stripes for large $J' = 0.05$ at doping $x = 0.25$.

VII. ACKNOWLEDGMENT

This work has been supported by the Austrian Science Fund (FWF), project no. P15834-PHY. We wish to thank the EPSRC (Grant GR/S18571/01) for financial support.

* Electronic address: daghofer@itp.tu-graz.ac.at

¹ T. Kaplan and S. Mahanti, *Physics of Manganites* (Kluwer Academic/ Plenum Publishers, New York, Boston, Dordrecht, London, Moscow, 1998), 1st ed.

² E. L. Nagaev, *Colossal Magnetoresistance and Phase Separation in Magnetic Semiconductors* (Imperial College Press, London, 2002), 1st ed.

³ C. Zener, *Phys. Rev.* **82**, 403 (1951).

⁴ P.-G. de Gennes, *Phys. Rev.* **118**, 141 (1960).

⁵ E. Dagotto, S. Yunoki, A. L. Malvezzi, A. Moreo, J. Hu, S. Capponi, D. Poilblanc, and N. Furukawa, *Phys. Rev. B* **58**, 6414 (1998).

⁶ N. Furukawa, *in: Physics of manganites* (Kluwer Academic Publisher, New York, 1998), 1st ed.

⁷ D. M. Edwards, *Adv. Phys.* **51**, 1259 (2002).

⁸ D. Meyer, C. Santos, and W. Nolting, *J. Phys. Condens. Matter* **13**, 2531 (2001).

⁹ W. Müller and W. Nolting, *Phys. Rev. B* **66**, 085205 (2002).

¹⁰ W. Koller, A. Prüll, H. G. Evertz, and W. von der Linden, *Phys. Rev. B* **66**, 144425 (2002).

¹¹ S. Yunoki and A. Moreo, *Phys. Rev. B* **58**, 6403 (1998).

¹² S. Yunoki, J. Hu, A. L. Malvezzi, A. Moreo, N. Furukawa, and E. Dagotto, *Phys. Rev. Lett.* **80**, 845 (1998).

¹³ H. Yi, N. H. Hur, and J. Yu, *Phys. Rev. B* **61**, 9501 (2000).

¹⁴ E. Dagotto, T. Hotta, and A. Moreo, *Phys. Rep.* **344**, 1 (2001).

¹⁵ Y. Motome and N. Furukawa, *J. Phys. Soc. Jpn.* **69**, 3785 (2000).

¹⁶ Y. Motome and N. Furukawa, *J. Phys. Soc. Jpn.* **72**, 2126 (2003).

¹⁷ W. Koller, A. Prüll, H. G. Evertz, and W. von der Linden, *Phys. Rev. B* **67**, 104432 (2003).

¹⁸ W. Koller, A. Prüll, H. G. Evertz, and W. von der Linden, *Phys. Rev. B* **67**, 174418 (2003).

¹⁹ H. Aliaga, B. Normand, K. Hallberg, M. Avignon, and B. Alascio, *Phys. Rev. B* **64**, 024422 (2001).

²⁰ S. Yunoki, A. Moreo, and E. Dagotto, *Phys. Rev. Lett.* **81**,

- 5612 (1998).
- ²¹ T. Hotta and E. Dagotto, Phys. Rev. B **61**, 11879 (2000).
- ²² T. Hotta, A. Feiguin, and E. Dagotto, Phys. Rev. Lett. **68**, 4922 (2001).
- ²³ Y. Motome and N. Furukawa, Phys. Rev. Lett. **91**, 167204 (2003).
- ²⁴ Y. Motome and N. Furukawa, Phys. Rev. (**68**, 144432 (2003).
- ²⁵ A. Moreo, S. Yunoki, and E. Dagotto, Science **283**, 2034 (1999).
- ²⁶ M. Moraghebi, C. Buhler, S. Yunoki, and A. Moreo, Phys. Rev. B **63**, 214513 (2001).
- ²⁷ M. Moraghebi, S. Yunoki, and A. Moreo, Phys. Rev. B **66**, 214522 (2002).
- ²⁸ M. Moraghebi, A. Moreo, and S. Yunoki, Phys. Rev. Lett. **88**, 187001 (2002).
- ²⁹ M. Daghofer, W. Koller, H. G. Evertz, and W. von der Linden, J. Phys.: Condens. Matter **16**, 1 (2004).
- ³⁰ D. F. Agterberg and S. Yunoki, Phys. Rev. B **62**, 13816 (2000).
- ³¹ M. Y. W. Koshibae and S. Maekawa, Phys. Rev. Lett. **81**, 5604 (1998).
- ³² E. Marinari, *Optimized monte carlo methods*, Lectures at the 1996 Budapest Summer School on Monte Carlo Methods (1996), URL cond-mat/9612010.
- ³³ K. Hukushima and K. Nemoto, cond-mat/9512035 (1995).
- ³⁴ K. Hukushima, H. Takayama, and K. Nemoto, Int. J. Mod. Phys. C **7**, 337 (1996).
- ³⁵ Y.-R. Chen and P. B. Allen, Phys. Rev. B **64**, 064401 (2001).
- ³⁶ D. S. Dessau, T. Saitoh, C. H. Park, Z. X. Shen, P. Villeda, N. Hamada, Y. Moritomo, and Y. Tokura, Phys. Rev. Lett. **81**, 192 (1998).
- ³⁷ T. Saitoh, D. S. Dessau, Y. Moritomo, T. Kimura, Y. Tokura, and N. Hamada, Phys. Rev. B **62**, 1039 (2000).
- ³⁸ Y.-D. Chuang, A. D. Gromko, D. S. Dessau, T. Kimura, and Y. Tokura, Science **292**, 1509 (2001).
- ³⁹ J.H. Park, C. T. Chen, S-W. Cheong, W. Bao, G Meigs, V. Chakarian, and Y. U. Idzerda, Phys. Rev. Lett **76**, 4215 (1996).
- ⁴⁰ M. Daghofer, W. Koller, W. von der Linden, and H. G. Evertz, cond-mat/0406635 (2004).